




**X-ray absorption linear dichroism at the Ti *K* edge of anatase TiO<sub>2</sub> single crystals**T. C. Rossi <sup>1</sup>, D. Grolimund,<sup>2</sup> M. Nachtegaal,<sup>3</sup> O. Cannelli,<sup>1</sup> G. F. Mancini,<sup>1</sup> C. Bacellar,<sup>1</sup> D. Kinschel,<sup>1</sup> J. R. Rouxel <sup>1</sup>, N. Ohannessian <sup>4</sup>, D. Pergolesi,<sup>4,5</sup> T. Lippert,<sup>4,6</sup> and M. Chergui<sup>1</sup><sup>1</sup>Laboratory of Ultrafast Spectroscopy, Ecole Polytechnique Fédérale de Lausanne SB-ISIC, and Lausanne Centre for Ultrafast Science (LACUS), Station 6, Lausanne, CH-1015, Switzerland<sup>2</sup>Laboratory for Femtochemistry - MicroXAS beamline project, Paul Scherrer Institute, Villigen, CH-5232, Switzerland<sup>3</sup>Bioenergy and Catalysis Laboratory, Paul Scherrer Institute, Villigen, CH-5232, Switzerland<sup>4</sup>Laboratory for Multiscale Materials Experiments, Paul Scherrer Institute, Villigen, CH-5232, Switzerland<sup>5</sup>Electrochemistry Laboratory, Paul Scherrer Institute, Villigen, CH-5232, Switzerland<sup>6</sup>Department of Chemistry and Applied Biosciences, Laboratory of Inorganic Chemistry, ETH Zürich, Vladimir-Prelog-Weg 1-5/10, 8093 Zürich, Switzerland

(Received 24 July 2019; revised manuscript received 25 October 2019; published 20 December 2019)

Anatase TiO<sub>2</sub> (a-TiO<sub>2</sub>) exhibits a strong x-ray absorption linear dichroism in the pre-edge, the XANES and the EXAFS at the titanium *K* edge. In the pre-edge region, the behavior of the A1–A3 and B peaks originating from the  $1s - 3d$  transitions is due to the strong *p*-orbital polarization and strong *p*–*d* orbital mixing. An unambiguous assignment of the pre-edge peak transitions is made in the mono-electronic approximation with the support of *ab initio* finite difference method calculations and spherical tensor analysis in quantitative agreement with the experiment. Our results suggest that several previous studies relying on octahedral crystal field splitting assignments are inaccurate due to the significant *p*-*d* orbital hybridization induced by the broken inversion symmetry in a-TiO<sub>2</sub>. It is found that A1 is mostly an on-site  $3d - 4p$  hybridized transition, while peaks A3 and B are nonlocal transitions, with A3 being mostly dipolar and influenced by the  $3d - 4p$  intersite hybridization, while B is due to interactions at longer range. Peak A2, which was previously assigned to a transition involving pentacoordinated titanium atoms, is shown to exhibit a quadrupolar angular evolution with incidence angle, which implies that its origin is primarily related to a transition to bulk energy levels of a-TiO<sub>2</sub> and not to defects, in agreement with theoretical predictions [Vorwerk *et al.*, *Phys. Rev. B* **95**, 155121 (2017)]. Finally, *ab initio* calculations show that the occurrence of an enhanced absorption at peak A2 in defect-rich a-TiO<sub>2</sub> materials originates from defect-related *p* density of states due to the formation of doubly ionized oxygen vacancies. The formation of peak A2 at almost the same energy for single crystals and nanomaterials is a coincidence while the origin is different. These results pave the way to the use of the pre-edge peaks at the Ti *K* edge of a-TiO<sub>2</sub> to characterize the electronic structure of related materials and in the field of ultrafast x-ray absorption spectroscopy where the linear dichroism can be used to compare the photophysics along different axes.

DOI: [10.1103/PhysRevB.100.245207](https://doi.org/10.1103/PhysRevB.100.245207)**I. INTRODUCTION**

Titanium dioxide (TiO<sub>2</sub>) is one of the most studied large-gap semiconductors due to its present and potential applications in photovoltaics [1] and photocatalysis [2]. The increasingly strict requirements of modern devices call for sensitive material characterization techniques which can provide local insights at the atomic level [3,4]. *K*-edge x-ray absorption spectroscopy (XAS) is an element-specific technique that is used to extract the local geometry around an atom absorbing the x radiation, as well as about its electronic structure [5]. A typical *K*-edge absorption spectrum usually consists of three parts: (i) In the high-energy region above

the absorption edge (typically > 50 eV), the extended x-ray absorption fine structure (EXAFS) contains information about bond distances. Modelling of the extended X-ray absorption fine structure (EXAFS) is rather straightforward, as the theory is well established [5]. (ii) The edge region and slightly above it (< 50 eV) represents the x-ray absorption near-edge structure (XANES), which contains information about bond distances and bond angles around the absorbing atom, as well as about its oxidation state. In contrast to EXAFS, XANES features require more complex theoretical developments due to the multiple scattering events and their interplay with bound-bound atomic transitions. (iii) The pre-edge region consists of bound-bound transitions of the absorbing atom. In the case of transition metals, the final states are partially made of *d* orbitals. Pre-edge transitions thus deliver information about orbital occupancies and about the local geometry because the dipole-forbidden *s* – *d* transitions are relaxed by lowering of the local symmetry. The Ti *K*-edge absorption spectrum of anatase TiO<sub>2</sub> (a-TiO<sub>2</sub>) exhibits four pre-edge features labeled A1, A2, A3, and B, while rutile TiO<sub>2</sub> only

Published by the American Physical Society under the terms of the [Creative Commons Attribution 4.0 International](https://creativecommons.org/licenses/by/4.0/) license. Further distribution of this work must maintain attribution to the author(s) and the published article's title, journal citation, and DOI.

shows three [6,7]. Their assignment has been at the center of a long debate, which is still going on, especially in the case of the a-TiO<sub>2</sub> polymorph [8–10]. In this paper, we use X-ray absorption spectroscopy (XAS) linear dichroism (LD) at the Ti *K* edge to assign the pre-edge transitions of a-TiO<sub>2</sub> since this technique can provide the orbital content in the final state of the bound transitions with the support of *ab initio* finite difference method (FDM) calculations and spherical tensor analysis of the absorption cross section.

Early theoretical developments to explain the pre-edge features in a-TiO<sub>2</sub> were based on molecular orbital (MO) theory [11–13], which showed that the first two empty states in a-TiO<sub>2</sub> are made of antibonding  $t_{2g}$  and  $e_g$  orbitals derived from the  $3d$  atomic orbitals of Ti. Transitions to these levels have, respectively, been assigned to the A3 and B peaks while the absorption edge is made of Ti  $t_{1u}$  antibonding orbitals derived from Ti  $4p$  atomic orbitals. Although MO theory can predict the energy position of the transitions accurately, it cannot compute the corresponding cross sections and does not account for the core hole to which quadrupolar transitions to  $d$ -orbitals at the *K* edge are extremely sensitive [9]. The corresponding transitions are usually redshifted by the core hole and appear as weak peaks on the low-energy side of the pre-edge. In a-TiO<sub>2</sub>, peak A1 contains a significant quadrupolar component [9], sensitive to the core hole, which explains the inaccuracy of MO theory to predict this transition. Full multiple scattering (FMS) is a suitable technique to treat large ensembles of atoms and obtain accurate cross sections [8,10,12,14]. From FMS calculations, a consensus has emerged assigning a partial quadrupolar character to A1, a mixture of dipolar and quadrupolar character with  $t_{2g}$  orbitals to A3, and a purely dipolar transition involving  $e_g$  orbitals to B [12,15]. However, as correctly pointed out by Ruiz-Lopez and Munoz-Paez [12], this simple picture of octahedral symmetry energy split  $t_{2g}$  and  $e_g$  levels becomes more complicated in a-TiO<sub>2</sub> because of the local distorted octahedral environment ( $D_{2d}$  symmetry), which allows local  $p-d$  orbital hybridization [16]. In that case, the dipolar contribution to the total cross section becomes dominant for every transition in the pre-edge region [17]. In addition, the cluster size used for the FMS calculations has a large influence on the A3 and B peak intensities, showing that delocalized final states (off-site transitions) play a key role in the pre-edge absorption region [12]. Finally, the local environment around Ti atoms in a-TiO<sub>2</sub> is strongly anisotropic and Ti-O bond distances separate into two groups of apical and equatorial oxygens which cannot be correctly described with spherical muffin-tin potentials as implemented in FMS. This limitation is overcome with the development of full potential FDM calculations for near-edge structure (FDMNES) [18–20].

Empirical approaches have been used by Chen *et al.* [21] and Luca *et al.* [7,22,23] to establish correlations between the Ti *K* pre-edge transitions in a-TiO<sub>2</sub> and sample morphologies, showing that bond length and static disorder contribute to the change in the pre-edge peak amplitudes [21] and that the A2 peak is due to pentacoordinated Ti atoms [7,22,23]. Farges *et al.* confirmed this assignment with the support of multiple scattering (MS) calculations [14]. The recent works by Zhang *et al.* [24] and Triana *et al.* [15] have shown the strong

interplay between the intensity of pre-edge features and the coordination number and static disorder, in particular in the case of the A2 peak. However, the A2 peak is also present in the XAS of single crystals, which suggests that the underlying transition is intrinsic to an almost defect-free a-TiO<sub>2</sub>. Clear evidence of the nature of this transition is lacking, which we provide in this paper.

The clear assignment of the pre-edge features of a-TiO<sub>2</sub> is important in view of recent steady-state and ultrafast XAS [25–27] and optical experiments [28]. In the picosecond XAS experiments on photoexcited a-TiO<sub>2</sub> nanoparticles above the band gap, a strong enhancement of the A2 peak was observed, along with a redshift of the edge [25]. This was interpreted as trapping of the electrons transferred to the conduction band (CB) at undercoordinated Ti centers that are abundant in the shell region of the nanoparticles, turning them from an oxidation state of +4 to +3 [25]. The trapping time was determined by femtosecond XAS to be < 200 fs, i.e., the electron is trapped immediately at or near the unit cell where it was created [26,27]. Further to this, the trapping sites were identified as being due to oxygen vacancies ( $O_{vac}$ ) in the first shell of the reduced Ti atom. These  $O_{vac}$ 's are linked to two Ti atoms in the equatorial plane and one Ti atom in the apical position to which the biexponential kinetics (hundreds of ps and a few ns) at the Ti *K*-edge transient was attributed [26,29]. However, this hypothesis awaits further experimental and theoretical confirmation. In this sense, the assignment of peak A2, which provides the most intense transient signal in the pre-edge of a-TiO<sub>2</sub> is a prerequisite.

In this paper, we provide a detailed characterization of the steady-state XAS spectrum by carrying out a LD study of a-TiO<sub>2</sub> single crystals at the Ti *K* edge, accompanied by detailed theoretical modeling of the spectra. We fully identify the four pre-edge bands (A1–A3 and B) beyond the octahedral crystal field splitting approximation used in several previous studies [17,30]. Their dipolar and quadrupolar character is analyzed in detail as well as their on-site vs intersite nature. We present a quantitative reproduction of the experimental LD data with FDM calculations, the observation of the quadrupolar nature of peak A2 in agreement with theoretical predictions [31], and the corresponding assignment of peak A2 as originating from a quadrupolar transition in single crystals and from defect states in nanomaterials. This delivers a high degree of insight into the environment of Ti atoms, which is promising for future ultrafast x-ray studies of the photoinduced structural changes in this material.

## II. EXPERIMENTAL SETUP

The LD measurements we performed at the microXAS beamline of the SLS in Villigen, Switzerland using a double Si(311) crystal monochromator to optimize the energy resolution. Energy calibration is performed from the first derivative of the XAS spectrum of a thin Ti foil. We used a moderately focused rectangular-shaped x-ray beam of  $20 \times 200 \mu\text{m}^2\text{m}^2$  in horizontal and vertical dimensions, respectively. The XAS spectrum is obtained in total fluorescence yield (TFY) with a Ketek Axas detector system with Vitus H30 SFF and ultralow capacitance Cube-Asic preamplifier (Ketek GmbH).

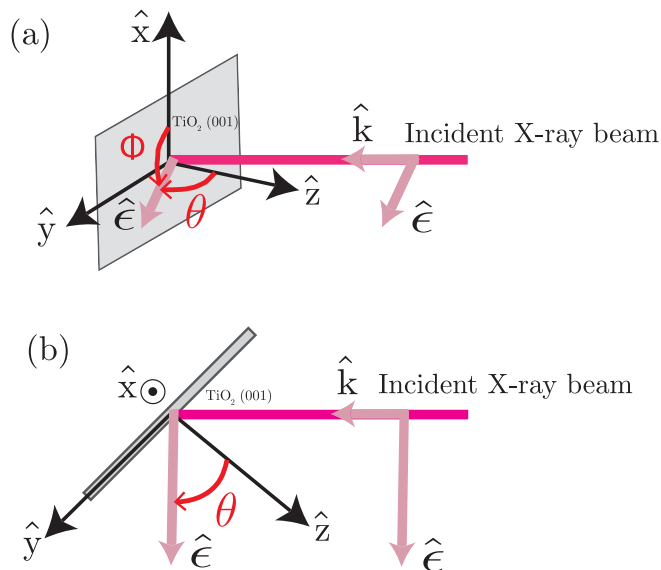


FIG. 1. Linear dichroism experiment with (a) side view and (b) top view. The sample surface is in grey while the incident x-ray beam is in pink. A set of Euler angles ( $\theta$ ,  $\phi$ ,  $\psi$ ) is used to orient the electric field  $\hat{\epsilon}$  and wave vector  $\hat{k}$  of the incident x-ray beam with respect to the sample.

The sample consists of a (001)-oriented crystalline  $\alpha$ -TiO<sub>2</sub> thin film of 30 nm thickness. Sample growth and characterization procedures are reported in the Supplemental Material (SM), Sec. 1 [32] (see also Refs. [33,34] therein). Figure 1 shows schematics of the sample motion required for the experiment. The sample was placed in the center of rotation of a system of stages which allow for both in-plane rotation ( $\phi$ ) and out-of-plane rotation ( $\theta$ ). By convention, a set of Euler angles ( $\theta$ ,  $\phi$ ,  $\psi$ ) orients the electric field  $\hat{\epsilon}$  and wave vector  $\hat{k}$  with respect to the sample.  $\theta$  measures the angle between  $\hat{\epsilon}$  and the [001] crystal direction ( $\hat{z}$  axis of the sample frame) orthogonal to the surface.  $\phi$  measures the angle between  $\hat{\epsilon}$  and the sample rotation axis  $\hat{x}$ . In principle, a third angle  $\psi$  is necessary to fix the position of the wave vector in the orthogonal plane to the electric field, but here  $\psi = 0^\circ$ . The  $\theta$  angles reported in the experimental data sets are with a maximum systematic offset of  $\pm 0.2^\circ$  which comes from the precision setting up the  $\theta = 0^\circ$  reference from the sample half clipping of the x-ray beam at grazing incidence. The precision of the rotation stage of  $\pm 0.01^\circ$  is negligible with respect to this angular offset.

LD is usually studied with the sample rotated in the plane orthogonal to the incident x-ray beam ( $\phi$ -rotation) [35]. In this paper, we present a sample rotation around  $\hat{x}$  ( $\theta$  rotation), which provides the largest changes in the XAS. This rotation induces a change of x-ray footprint onto the sample surface. We clearly show that it does not introduce spectral distortions because the effective penetration depth of the x rays through the material (between 97 and 580 nm across the absorption edge of  $\alpha$ -TiO<sub>2</sub> for the largest footprint at  $\theta = 1^\circ$  used here [36]) is kept constant as the sample is much thinner than the attenuation length at the Ti  $K$  edge. Instead, the total amount of material probed by the x rays changes due to the larger x-ray footprint when  $\theta$  increases and a renormalization over

the detected number of x-ray fluorescence photons is required. This is done with the support of the FDMNES calculations since a few energy points have  $\theta$ -independent cross sections, as previously reported in other systems [37–43] (*vide infra*) [44]. With this renormalization procedure performed at a single energy point (4988.5 eV), we could obtain a set of experimental points with  $\theta$ -independent cross sections at the energies predicted by the theory confirming the reliability of the method. Hence, crystalline thin films with suitable thicknesses with respect to the x-ray penetration depth offer more possibilities to study LD effects than single crystals and prevent the usual self-absorption distortion of bulk materials when using TFY detection [45].

### III. THEORY

#### A. Recent developments in computational methods

Recently, there have been two main developments in the computation of XANES spectra. The first is based on band-structure calculations (LDA, LDA + U, ...), which compute potentials self-consistently with and without the core hole before the calculation of the XAS absorption cross section with a core hole in the final state [17,46]. This approach provides excellent accuracy but is limited to the few tens of eV above the absorption edge due to the computational cost of increasing the basis set to include the EXAFS. The second one, the FDMNES approach implemented by Joly *et al.* [19,20], overcomes the limitations of the muffin-tin approximation to get accurate descriptions of the pre-edge transitions, especially for anisotropic materials. The recent theoretical work by Cabaret *et al.* combining GGA-PBE self-consistent calculations with FDMNES [17] concluded that in  $\alpha$ -TiO<sub>2</sub>, peak A1 is due to a mixture of quadrupolar ( $t_{2g}$ ) and dipolar transitions ( $p - t_{2g}$ ), A3 to on-site dipolar ( $p - e_g$ ), off-site dipolar ( $p - t_{2g}$ ) and quadrupolar ( $e_g$ ) transitions, while B is due to an off-site dipolar transition ( $p_z - e_g$ ). These results, together with those of previous works, are summarized in Table I. However, experimental support to the pre-edge assignments is still lacking, and is provided in this paper using Ti  $K$  edge LD XAS spectra with the theoretical support of *ab initio* full-potential FDMNES calculations and spherical harmonics analysis of the XAS cross section.

#### B. Finite difference *ab - initio* calculations

The *ab-initio* calculations of the XAS cross section were performed with the full potential FDM as implemented in the FDMNES package [18,19]. A cluster of 7.0 Å was used for the calculation with the fundamental electronic configuration of the oxygen atom and an excited state configuration for the titanium atom (Ti : [Ar]3d<sup>1</sup>4s<sup>2</sup>4p<sup>1</sup>) as performed elsewhere [24]. We checked the convergence of the calculation for increasing cluster sizes and found minor evolution for larger cluster radii than 7.0 Å (123 atoms). The Hedin-Lundqvist exchange-correlation potential is used [47]. A minor adjustment of the screening properties of the 3d levels is needed to match the energy position of the pre-edge features with the experiment. We found the best agreement for a screening of 0.85 for the 3d electrons. After the convolution of the spectrum with an arctan function with maximum broadening of 1.5 eV, a constant

TABLE I. Previous and present assignments of the final states involved in the Ti *K* pre-edge transitions of a-TiO<sub>2</sub> single crystals. The orbitals with dominant contribution to the transition are emphasized in bold. *E*1 is for dipolar transitions and *E*2 for quadrupolar transitions. Off-site transitions are in red, on-site transitions are in black. Irreducible representations corresponding to the final state in the considered point group of a-TiO<sub>2</sub> are in parentheses. The dash (–) symbol refers to orbital hybridization.

Reference	A1	A2	A3	B
[10]	<b>3d<sub>x<sup>2</sup>-y<sup>2</sup></sub></b> (b <sub>1</sub> ), 4p <sub>x</sub> , 4p <sub>y</sub> , 3d <sub>xz</sub> , 3d <sub>yz</sub> (e)	<b>4p<sub>z</sub>, 3d<sub>xy</sub></b> (b <sub>2</sub> ), 4p <sub>x</sub> , 4p <sub>y</sub> , 3d <sub>xz</sub> , 3d <sub>yz</sub> (e)	<b>4p<sub>z</sub>, 3d<sub>xy</sub></b> (b <sub>2</sub> ), 3d <sub>z<sup>2</sup></sub> (a <sub>1</sub> )	<b>4p, 4s</b>
[17]	<i>E</i> 1: <b>p(t<sub>2g</sub>)</b> , <i>E</i> 2: 3d(t <sub>2g</sub> )		<i>E</i> 1: <b>p(e<sub>g</sub>)</b> , <b>p – 3d(t<sub>2g</sub>)</b> , <i>E</i> 2: 3d(e <sub>g</sub> )	<i>E</i> 1: <b>p<sub>z</sub>, 3d(e<sub>g</sub>)</b>
[15]	<i>E</i> 1: <b>4p – 3d(t<sub>2g</sub>)</b> , <i>E</i> 2: 3d(t <sub>2g</sub> )		<i>E</i> 1: <b>4p, d<sub>xy</sub>, d<sub>xz</sub>, d<sub>yz</sub></b> (t <sub>2g</sub> )	<i>E</i> 1: <b>4p, d<sub>x<sup>2</sup>-y<sup>2</sup></sub>, d<sub>z<sup>2</sup></sub></b> (e <sub>g</sub> )
This work	<i>E</i> 1: <b>4p<sub>x,y</sub> – 3d<sub>xz</sub>, 3d<sub>yz</sub></b> , <i>E</i> 2: d <sub>xz</sub> , d <sub>yz</sub> , d <sub>x<sup>2</sup>-y<sup>2</sup></sub>	<i>E</i> 1: 4p <sub>z</sub> – 3d <sub>xy</sub> , <i>E</i> 2: <b>3d<sub>xy</sub>, 3d<sub>z<sup>2</sup></sub></b>	<i>E</i> 1: <b>4p<sub>x</sub>, 4p<sub>y</sub>, 4p<sub>z</sub> – 3d<sub>xy</sub>, 3d<sub>z<sup>2</sup></sub></b>	<i>E</i> 1: <b>4p<sub>x</sub>, 4p<sub>y</sub>, 4p<sub>z</sub></b>

gaussian broadening of 0.095 eV is applied to account for the experimental resolution of the experiment and get the closest agreement with the broadening of the pre-edge peaks.

### C. Spherical tensor analysis of the dipole and quadrupole cross sections

Analytical expressions of the dipole and quadrupole XAS cross sections [ $\sigma^D(\hat{\epsilon})$  and  $\sigma^Q(\hat{\epsilon}, \hat{k})$ , respectively] are obtained from their expansion into spherical harmonic components [35,48]. The expressions of  $\sigma^D(\hat{\epsilon})$  and  $\sigma^Q(\hat{\epsilon}, \hat{k})$  depend on the crystal point group which is D<sub>4h</sub> (4/*mmm*) for a-TiO<sub>2</sub>. The dipole cross section is given by

$$\sigma^D(\hat{\epsilon}) = \sigma^D(0, 0) - \frac{1}{\sqrt{2}}(3 \cos^2 \theta - 1)\sigma^D(2, 0) \quad (1)$$

and the quadrupole cross section by

$$\begin{aligned} \sigma^Q(\hat{\epsilon}, \hat{k}) = & \sigma^Q(0, 0) \\ & + \sqrt{\frac{5}{14}}(3 \sin^2 \theta \sin^2 \psi - 1)\sigma^Q(2, 0) \\ & + \frac{1}{\sqrt{14}}[35 \sin^2 \theta \cos^2 \theta \cos^2 \psi \\ & + 5 \sin^2 \theta \sin^2 \psi - 4]\sigma^Q(4, 0) \\ & + \sqrt{5} \sin^2 \theta[(\cos^2 \theta \cos^2 \psi - \sin^2 \psi) \cos 4\phi \\ & - 2 \cos \theta \sin \psi \cos \psi \sin 4\phi]\sigma^{Qr}(4, 4), \quad (2) \end{aligned}$$

with  $\theta$ ,  $\phi$ , and  $\psi$  as defined in the Ti site point group (D<sub>2d</sub>).  $\sigma^X(l, m)$  with  $X = D, Q$  is the spherical tensor with rank  $l$  and projection  $m$ .  $\sigma^{Xr}$  refers to the real part of the cross-section. The Euler angles ( $\theta$ ,  $\phi$ ,  $\psi$ ) in the experiment are referenced to the crystal frame, which is rotated in the ( $O, \hat{x}, \hat{y}$ ) plane with respect to the Euler angles in the Ti site frame. Consequently, the angles in Eqs. (1) and (2) differ from the angles defined in Fig. 1 by a rotation of  $\phi$ . In the Ti site frame, the  $\hat{x}$  and  $\hat{y}$  axes are bisectors of the Ti-O bonds while the crystal frame is along the bonds. The matrix  $R$  to go from the site frame to the crystal frame is

$$R = \begin{pmatrix} \frac{1}{\sqrt{2}} & \frac{1}{\sqrt{2}} & 0 \\ -\frac{1}{\sqrt{2}} & \frac{1}{\sqrt{2}} & 0 \\ 0 & 0 & 1 \end{pmatrix}. \quad (3)$$

In the following, the polarizations of  $\hat{\epsilon}$  and  $\hat{k}$  are given in the crystal frame. Consequently, the corresponding polarizations for the site frame are given by  $\hat{\epsilon}_S = R^{-1}(\hat{\epsilon})$  and  $\hat{k}_S = R^{-1}(\hat{k})$ .

Although some terms of  $\sigma^D(\hat{\epsilon})$  and  $\sigma^Q(\hat{\epsilon}, \hat{k})$  may be negative, the total dipolar and quadrupolar cross sections must be positive, putting constraints on the values of  $\sigma^D(l, m)$  and  $\sigma^Q(l, m)$ . The electric field  $\hat{\epsilon}$  and wave-vector  $\hat{k}$  coordinates in the ( $\hat{x}, \hat{y}, \hat{z}$ ) basis of Fig. 1 are given by

$$\hat{\epsilon} = \begin{pmatrix} \sin \theta \cos \phi \\ \sin \theta \sin \phi \\ \cos \theta \end{pmatrix}, \quad \hat{k} = \begin{pmatrix} \cos \theta \cos \phi \\ \cos \theta \sin \phi \\ -\sin \theta \end{pmatrix}. \quad (4)$$

Hence the detail of the cross-section angular dependence in Eqs. (1) and (2) requires the estimate of the spherical tensors  $\sigma^D(l, m)$  and  $\sigma^Q(l, m)$  as performed elsewhere [33]. The XAS cross section measured experimentally is an average over equivalent Ti atoms under the symmetry operations of the crystal space group. The analytical formula representing this averaged cross section requires the site symmetrization and crystal symmetrization of the spherical tensors, which is provided in the SM, Secs. 7 and 8 [32]. From this analysis, we obtain nearly equal (up to a sign difference) crystal-symmetrized [ $\langle \sigma(l, m) \rangle_X$ ], site-symmetrized [ $\langle \sigma(l, m) \rangle$ ], and standard [ $\sigma(l, m)$ ] spherical tensors. Assuming pure 3d and 4p final states in the one-electron approximation, analytical expressions are provided for  $\sigma^D(\hat{\epsilon})$  and  $\sigma^Q(\hat{\epsilon}, \hat{k})$  whose angular dependence with  $\theta$  and  $\phi$  are given in Table II. The full expressions of the cross sections are provided in the SM, Sec. 7 [32]. In this paper, we analyze the angular dependence of the pre-edge peak intensities with  $\theta$  and  $\phi$  and assign them to specific final states corresponding to Ti-3d and/or 4p orbitals with the support of both FDM and spherical tensor analysis.

## IV. RESULTS

The experimental evolution of the Ti *K*-edge spectra with  $\theta$  is depicted in Figs. 2(a) and 2(b). The spectra are normalized at 4988.5 eV where the cross section is expected to be  $\theta$ -independent according to FDMNES calculations [shown by the leftmost black arrow in Fig. 2(c)]. From this normalization procedure, a series of energy points with the cross-section independent of the  $\theta$  angle appear in the experimental data set, as predicted by theory [black arrows in Figs. 2(a) and 2(c)], showing the reliability of the normalization procedure. In the pre-edge, the amplitude of peak A1 is dramatically affected

TABLE II. Angular dependence along  $\theta$  and  $\phi$  of the dipole and quadrupole XAS cross-section dominant terms in Eqs. (1) and (2) at the Ti  $K$ -edge of  $\alpha$ -TiO<sub>2</sub>, according to the final state of the transition. Transitions to  $p$  final states are dipole allowed [ $\sigma^D(\hat{\epsilon})$ ], while transitions to  $d$  final states are quadrupole allowed [ $\sigma^Q(\hat{\epsilon}, \hat{k})$ ].

Final state	$\sigma^D(\hat{\epsilon})$ or $\sigma^Q(\hat{\epsilon}, \hat{k})\theta$ dependence	$\sigma^D(\hat{\epsilon})$ or $\sigma^Q(\hat{\epsilon}, \hat{k})\phi$ dependence
$p_x, p_y$	$-\cos^2 \theta$	no dependence
$p_z$	$\cos^2 \theta$	no dependence
$d_{z^2}$	$\sin^2 \theta \cos^2 \theta$	no dependence
$d_{xy}$	$\sin^2 \theta \cos^2 \theta$	$\cos(4\phi)$
$d_{x^2-y^2}$	$\sin^2 \theta \cos^2 \theta$	$-\cos(4\phi)$
$d_{xz}, d_{yz}$	$-\sin^2 \theta \cos^2 \theta$	no dependence

by the sample orientation. In the post-edge regions, significant changes are observed as well.

*Ab initio* FDM calculations of the total XAS cross section (including dipolar and quadrupolar terms) are presented in Figs. 2(c) and 2(d) for the same angles of incidence  $\theta$  as in

the experiment. In the pre-edge region, the trends for peak A1 and A3 are nicely reproduced. The absence of peak A2 at first sight, partially originating from defects [7,21–23], is due to our perfect crystal modeling in the FDM calculations. In the post-edge region, a good agreement is found, especially for the

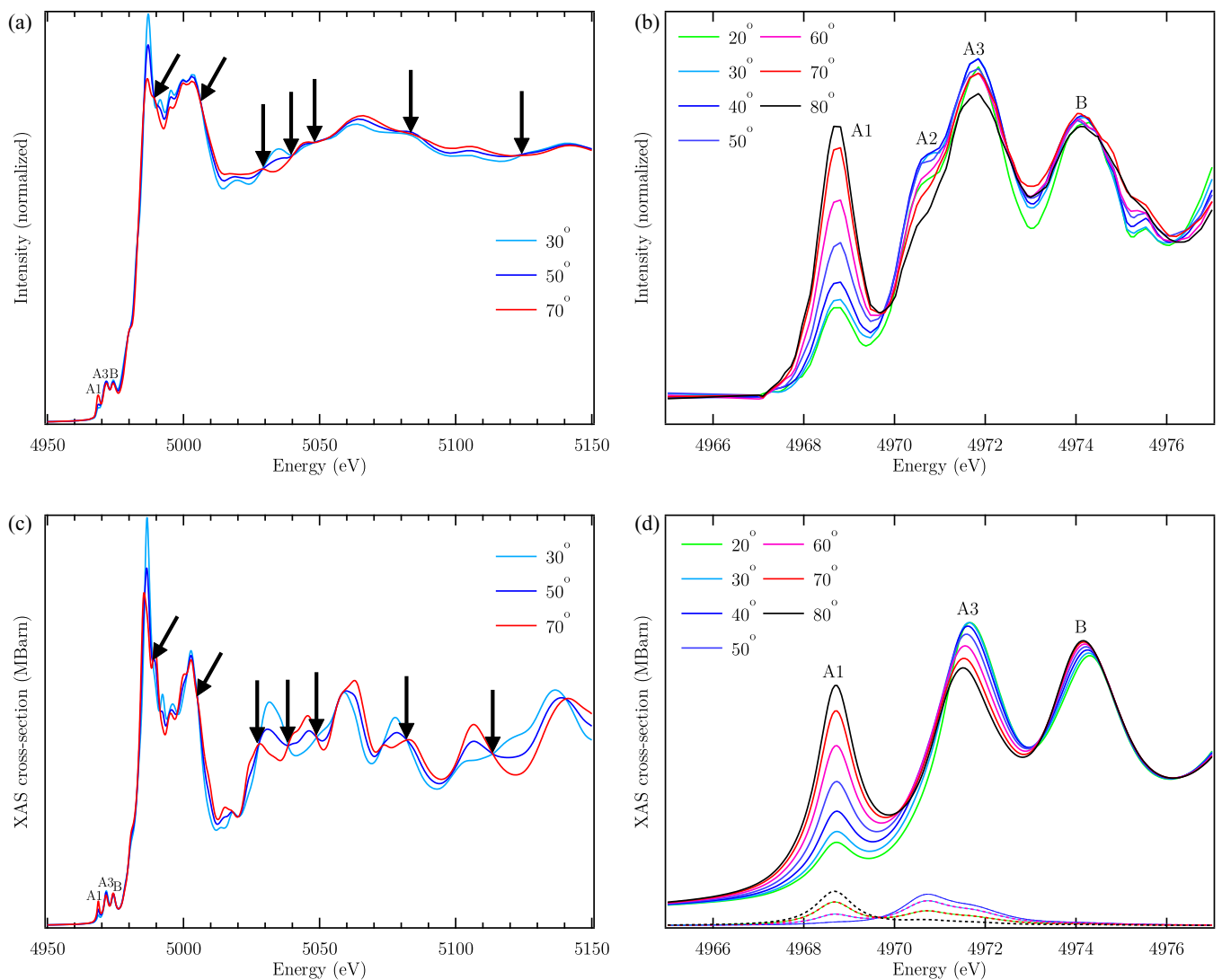


FIG. 2. (a), (b) Experimental and (c), (d) calculated Ti  $K$  edge spectra at the of  $\alpha$ -TiO<sub>2</sub> for different angles of incidence  $\theta$  with the sum of dipolar and quadrupolar components (thick lines) and with quadrupolar components only [thin lines and dashed lines in (d) for better visibility of overlapping curves]. The full x-ray absorption spectrum is shown in (a), (c) while the pre-edge region is shown in (b), (d). A few points with  $\theta$ -independent cross sections are marked with black arrows.

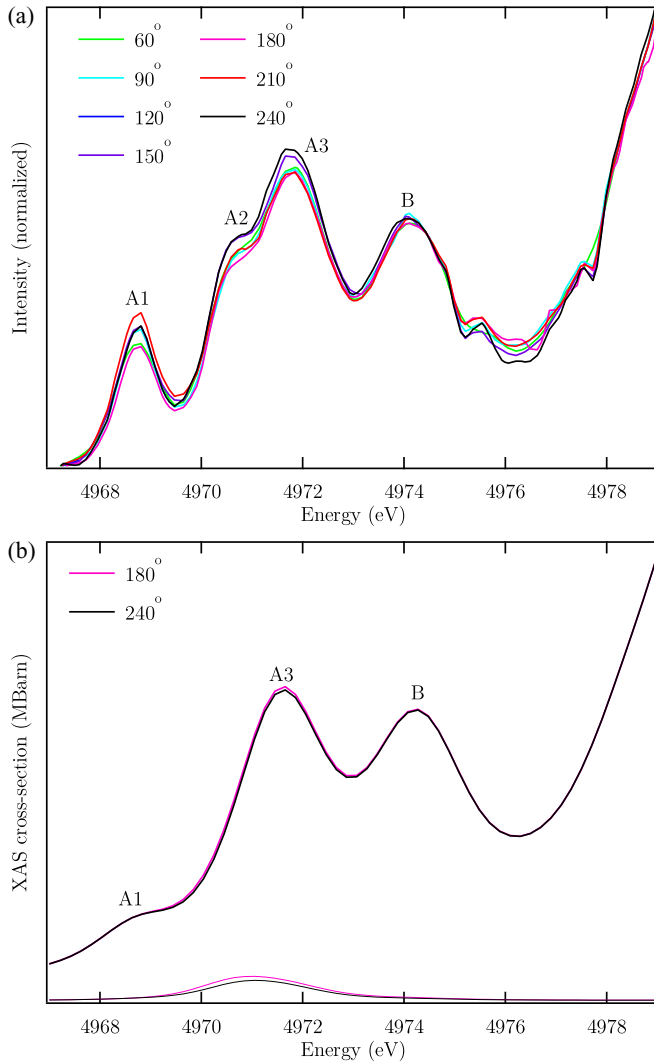


FIG. 3. (a) Experimental and (b) calculated XAS spectra at the Ti K pre-edge region of a-TiO<sub>2</sub> for different sample orientations along  $\phi$  ( $\theta = 45^\circ$ ) with the sum of dipolar and quadrupolar components (thin lines) and with quadrupolar components only [thin dashed lines in (b)]. Only two spectra are shown in (b) because only two different spectra can be sampled in  $30^\circ$  steps due to the periodicity of  $90^\circ$  of quadrupolar transitions.

isosbestic points. This shows that a strong LD remains well above the edge in this material.

The evolution of the spectra is also shown for a fixed incidence angle  $\theta = 45^\circ$  while the sample is rotated around  $\phi$  [Fig. 3(a)] [49]. The changes in amplitude are significantly less than with  $\theta$  rotation. We observe a minimal evolution of the amplitudes of peak B and at the rising edge from 4971 eV while a larger effect is distinguished in the spectral region of peaks A1, A2, and A3. *Ab initio* calculations with the same  $\hat{\epsilon}$  and  $\hat{k}$  orientations as in the experiment are depicted in Fig. 3(b). Only a weak evolution of the amplitude of the pre-edge features is expected and is essentially located in the region of peaks A2 and A3. The amplitude should reach its maximum for  $\phi = 180^\circ$  [90°], which is inconsistent with the experiment. Instead, the fitted evolution of the pre-edge peak amplitudes shows that A2 undergoes a 30% peak am-

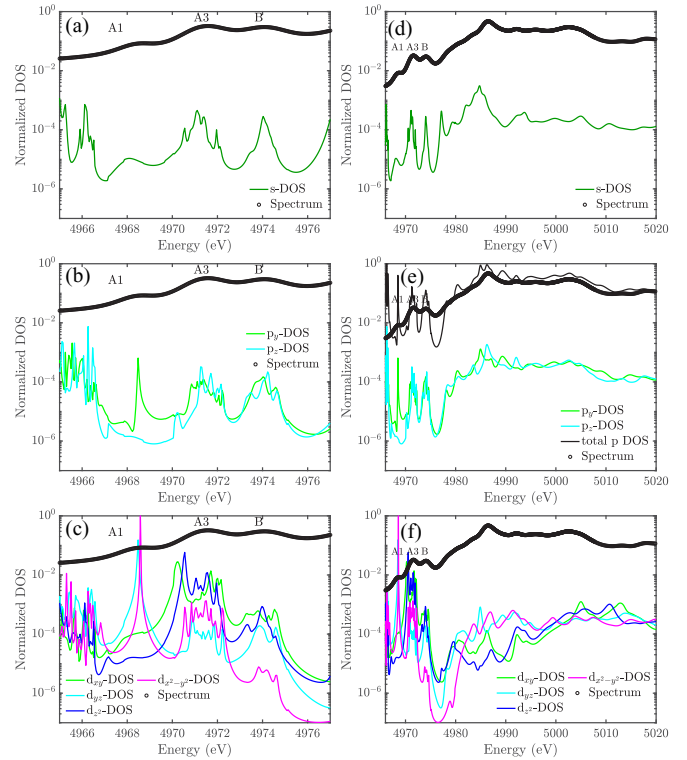


FIG. 4. Calculated projected final state DOS for each type of (a), (d) *s*-, (b), (e) *p*- and (c), (f) *d*-final state orbitals in the pre-edge (left) and postedge (right) regions. Reported spectra (black circles) are calculated for  $\theta = 90^\circ$ . The total *p* DOS ( $p_x, p_y, p_z$ ) is given in (e) (black line).

plitude change whose angular variation is compatible with a quadrupolar transition (SM, Fig. 6(a) [32]) while A1, A3, and B have a maximum amplitude evolution of 10% (within the fitting confidence interval) with no specific periodicity (SM, Fig. 7 [32]). The strong variation in A2 peak amplitude can be observed by the appearance of a pronounced shoulder for  $\phi = 150^\circ$ , which becomes smoother for  $\phi = 180^\circ$  [Fig. 3(a)]. Consequently, the main evolution in the pre-edge under  $\phi$  rotation is due to peak A2 which explains the disagreement with the perfect crystal FDM calculations. It also shows the essentially dipolar content of peaks A1, A3, and B, providing circles in polar plots along  $\phi$  (SM, Fig. 7 [32]), which is in agreement with the results obtained from  $\theta$  scans (*vide infra*). A fit of the A2 peak with a  $90^\circ$ -periodic function shows that it may be assigned to the contribution of  $d_{x^2-y^2}$  orbitals from the expected angular evolution by spherical harmonic analysis (SM, Figs. 6(a) and 6(b) [32]). However, the  $d_{x^2-y^2}$  density of states (DOS) in the region of peak A2 is negligible with respect to  $d_{xy}$  and  $d_{z^2}$  (*vide supra*), hence we rely on the more pronounced angular evolution with  $\theta$  in the following to show the involvement of  $d_{xy}$  orbitals in the formation of peak A2.

To describe the origin of the LD dependence with  $\theta$  and assign the pre-edge resonances, the projected DOS of the final states for the pre-edge and postedge region is depicted in Fig. 4 (we drop the term “projected” in the following for simplicity). Due to the large differences between the DOS of *s*, *p*, and *d* states, a logarithmic scale is used vertically and normalized to the orbital having the largest DOS contributing

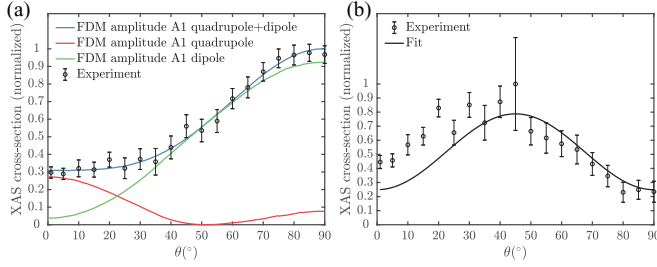


FIG. 5. Overlap between the angular evolution of the amplitudes for peaks (a) A1, (b) A2 in the theory (lines) and the experiment (circles with error bars). The error bars represent 95% of confidence interval for the fitting of the amplitude.

to the final state among  $s$ ,  $p$ , and  $d$  orbitals. For peaks A1, A3, and B, most of the DOS comes from  $d$  orbitals while the  $s$  and  $p$  DOS's are comparable. However, due to the angular momentum selection rule, the spectrum resembles the  $p$  DOS both in the pre-edge and the postedge regions as witnessed by the similarity between the total  $p$  DOS and the calculated spectrum [black line in Fig. 4(e)]. Importantly, peak A1 has only  $(p_x, p_y)$  contributions [Fig. 4(b)], meaning that this transition is expected to have a much weaker intensity when the electric field becomes parallel to the  $\hat{z}$  axis, in agreement with the  $\theta$  dependence of its amplitude (Fig. 2). The  $d$  DOS at peak A1 involves  $d_{xz}$ ,  $d_{yz}$ , and  $d_{x^2-y^2}$  orbitals [Fig. 4(c)], among which the first two can hybridize with the  $(p_x, p_y)$  orbitals and relax the dipole selection rules. The dipolar nature of A1 is also seen from the monotonic increase of its amplitude from  $\theta = 0^\circ$  to  $\theta = 90^\circ$ , inconsistent with a quadrupolar-allowed transition with  $90^\circ$  periodicity. Following the same analysis, peaks A3 and B do not undergo a strong change in amplitude under  $\theta$  rotation because  $(p_x, p_y)$  and  $p_z$  contribute similarly to the DOS for these transitions [Fig. 4(b)] although FDM calculations show that A3 should evolve in intensity with  $\theta$  due to a  $\sim 20\%$  larger DOS for  $p_z$  than for  $p_x, p_y$  as experimentally observed. From the integrated  $d$  DOS along  $(x, y)$  and  $z$  (SM Fig. 8(a) [32]), we notice the inconsistency between the peak amplitudes in the theory and the experiment, which shows that they are essentially determined by the  $p$  DOS (SM Fig. 8(b) [32]).

For a more quantitative description of the dipolar and quadrupolar components in the pre-edge, we extracted the quadrupolar cross section from the FDM calculations. It is shown as thin lines in Fig. 2(d), where continuous and dashed lines are used for better visibility of overlapping curves. The quadrupolar contributions are limited to peaks A1 and A3 with a contribution in the spectral region of peak A2. At peak A1, the quadrupolar amplitude is maximum for  $\theta = 0^\circ$  and  $\theta = 90^\circ$  and the total cross section becomes mainly quadrupolar for  $\theta = 0^\circ$  while the quadrupolar component contributes  $\sim 15\%$  of the peak amplitude for  $\theta = 90^\circ$ . From the development of the cross section into spherical harmonics (Table II), the dipolar transitions to  $p_{x,y}$  final states are expected to vary as  $-\cos^2\theta$  while transitions to  $p_z$  vary as  $\cos^2\theta$  plus a constant (see SM, Fig. 12(a) [32]). The fitted evolution of the dipolar cross section of peak A1 in the experiment and in the FDM calculations is compatible with a transition to  $p_{x,y}$  (green line in Fig. 5(a), fitting details in

the SM, Sec. 2 [32]). The quadrupolar component [red line in Fig. 5(a)] is compatible with a transition to  $d_{xz}, d_{yz}$  due to its  $-\sin^2\theta \cos^2\theta$  predicted evolution (Table II) in agreement with the  $d$  DOS at peak A1 [Figs. 4(c) and 12(b) in the SM] [32]. The comparison between the experimental and theoretical amplitudes of peak A1 [Fig. 5(a)] gives excellent agreement, further confirming that the A1 transition is mostly dipolar to  $p_{x,y}$  final states. Following the same analysis, it is more difficult to determine the dominant  $p$  DOS contributing to the transitions at peak A3 and B due to the weak evolution of their amplitude with  $\theta$ .

As pointed out earlier, the quadrupolar cross section has a doublet structure in the region of peaks A2 and A3 [Fig. 2(d)]. The most intense of the two peaks at  $\theta = 45^\circ$  is in the spectral region of peak A2 where the transition involving defects is expected in a-TiO<sub>2</sub> nanoparticles, for instance. A closer look at the fitted evolution of the A2 amplitude with  $\theta$  shows a quadrupolar evolution with maximum value at  $\theta = 45^\circ$  [Fig. 5(b)]. This is in agreement with the expected angular evolution of  $d_{z^2}$  and  $d_{xy}$  final states from spherical tensor analysis (SM, Fig. 12(b) [32]) which contribute to the DOS in the spectral region of peak A2 [Fig. 4(c)]. It indicates that although the amplitude of A2 is underestimated in the FDM calculations, the consensus that A2 originates from undercoordinated and disordered samples may be more subtle because of the involvement of a transition in the perfect crystal as discussed below.

From this combined experimental and theoretical analysis, we emphasize that consecutive peaks in the pre-edge of a-TiO<sub>2</sub> are not simply due to the energy splitting between  $t_{2g}$  and  $e_g$  as previously invoked [17]. This splitting is more complicated than the usual octahedral crystal field splitting because of the strong hybridization between  $p$  and  $d$  orbitals in a lowered symmetry environment, which affects the relative ordering of the transitions. The consistent results between experiment, FDM calculations, and spherical tensor analysis show the reliability of the assignment provided in this paper. Table I compares our results with previous assignments of peaks A1 to B.

## V. DISCUSSION

### A. Local versus nonlocal character of the pre-edge transitions

Pre-edge transitions can originate either from on-site (localized) or off-site transitions involving neighbor Ti atoms of the absorber. Off-site transitions are dipole allowed due to the strong  $p-d$  orbital hybridization [16]. This effect has been shown on NiO, an antiferromagnetic (AF) charge-transfer insulator, for which the Ni  $K$ -edge transition to  $3d$  orbitals of the majority spin of the absorber is only possible between Ni sites due to the AF ordering [46]. Hence, to disentangle between the local or nonlocal character of the pre-edge transitions in a-TiO<sub>2</sub>, we performed FDM calculations on clusters with an increasing number of neighbor shells starting from an octahedral TiO<sub>6</sub> cluster with the same geometry and bond distances as in the bulk. The results are shown in Fig. 6 with two orthogonal electric field orientations along [001] ( $\theta = 0^\circ$ ) and [010] ( $\theta = 90^\circ$ ).

The calculation for TiO<sub>6</sub> (green curve) shows only A1, meaning that it is mostly an on-site transition. The absence

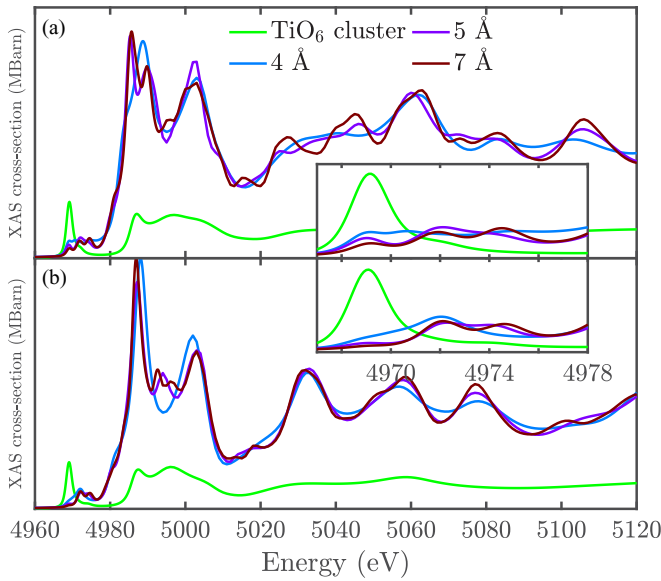


FIG. 6. Evolution of the calculated a-TiO<sub>2</sub> XAS spectrum at the Ti *K* edge with cluster size in the FDM calculation for (a)  $\theta = 90^\circ$  ( $\hat{\epsilon} \parallel [010]$ ,  $\hat{k} \parallel [00-1]$ ), (b)  $\theta = 0^\circ$  ( $\hat{\epsilon} \parallel [001]$ ,  $\hat{k} \parallel [100]$ ).

of peaks A3 and B suggests that they are mostly nonlocal transitions in agreement with Ref. [17]. Increasing the cluster size to 4 Å includes the second shell of Ti ions, which generates most of the A3 amplitude. This shows that, similar to NiO, an energy gap opens between the on-site and off-site transitions to 3*d* orbitals of Ti and that A3 is mostly dipolar and strongly influenced by the intersite 3*d* – 4*p* hybridization. Peak B is missing for this cluster size which shows that it is due to a longer range interaction and can be reconstructed with a 5 Å cluster, including the next shell of neighbor Ti atoms. A similar trend in the local or nonlocal character of the pre-edge transitions is observed at the metal *K* edge of 3*d* transition metal oxides which has to do with the degree of *p* – *d* orbital mixing [30].

### B. Origin of peak A2 in bulk a-TiO<sub>2</sub>

The experimental  $\phi$  and  $\theta$  angular evolution of the A2 amplitude (Figs. 5(b) and 6(a) in the SM [32]) matches a quadrupolar transition and qualitatively consistent with the cross section obtained from FDMNES calculations in the region of peak A2 [thin lines in Figs. 2(d) and 3(b)]. Recent calculations accounting for the electron-hole interaction in the Bethe-Salpeter equation have reproduced peak A2, although with an underestimated amplitude as in our FDM calculations [31]. Peaks A1 and A2 are found to exhibit their maximum amplitude when the electric field is parallel to the (a, b) and c axes, respectively. This is in agreement with our measurement for peak A1 [Fig. 5(a)] as a result of the coupling between the 3*d* orbitals of Ti with the *p*<sub>*x,y*</sub> DOS. For peak A2 [Fig. 5(d)], we observe a dominant quadrupolar evolution with a deviation from the ideal behavior showing the presence of *p*<sub>*z*</sub> states, which increase their contribution to the transition when  $\theta \rightarrow 0^\circ$  (see blue line in the SM, Fig. 12(a) [32]). Although both peaks A1 and A2 show *p*-*d* orbital mixing, this mixing is clearly stronger for the A1 peak where the dipole contribution

becomes dominant over the quadrupolar in contrast to the A2 peak. It shows that the amount of *p*-*d* orbital mixing differs for these transitions, which can be explained by the  $\sim 100$  times lower *p*<sub>*z*</sub> DOS in the region of peak A2 than *p*<sub>*x,y*</sub> DOS in the region of peak A1 [Fig. 4(b)]. The underestimated amplitude of peak A2 in our calculation is likely due to the lack of explicit treatment of the electron-hole interaction, which would improve the agreement of energy and amplitudes for peaks A1 and A2 without resorting to changes in screening constants of the 3*d* electrons as in our study. Recent calculations using the Bethe-Salpeter equation estimate that the average amplitude of peak A2 is  $\sim 15\%$  of the average amplitude of peak A1, which comforts this hypothesis [31]. A parallel can be made between the energy splitting of peaks A1 and A2 containing quadrupolar localized components and the splitting of the bound excitons of a-TiO<sub>2</sub> observed in the optical range where the (a, b) plane exciton has a larger binding energy than the c exciton [28,50,51].

### C. Origin of peak A2 in defect-rich a-TiO<sub>2</sub>

While we show that the presence of the A2 peak can be explained by the electronic structure of a-TiO<sub>2</sub>, a number of previous studies have concluded that A2 is related to lattice defects [7,21–23,25,26,29]. The question arises as to the connection between the A2 peak and the lattice defects, if any. Oxygen vacancies are native defects in a-TiO<sub>2</sub> [52]. The occurrence of an oxygen vacancy (*O*<sub>vac</sub>) in the vicinity of a Ti atom will further lower the *D*<sub>2*d*</sub> symmetry and introduce *p* – *d* orbital mixing in the pentacoordinated Ti atom increasing the transition amplitude while broadening the transition due to the inhomogeneous contribution of the vacancy distribution [15,24]. To check the effect of an *O*<sub>vac</sub> on the XAS spectrum of a Ti atom in the vicinity, *ab initio* FDM calculations are performed at the Ti *K* edge of Ti atoms with a doubly ionized *O*<sub>vac</sub> (*V*<sub>O</sub><sup>2+</sup>) at the apical or equatorial position in a supercell of 768 atoms. The calculations are performed with a bulk a-TiO<sub>2</sub> 4 × 4 × 4 superlattice structure from which one oxygen atom is removed in the center and neighbor titanium atoms are moved along the broken Ti–O bond to simulate lattice relaxation. We have taken the local structural relaxation reported in another work with hybrid functional calculations where the titanium atoms move away from *V*<sub>O</sub><sup>2+</sup> by 0.509 Å in the equatorial plane and 0.109 Å in the apical position [53]. The results are depicted in Fig. 7(a) for the absorption cross section and Fig. 7(b) for the DOS [54]. The calculations with an oxygen vacancy show a peak in the region between peak A1 and peak A3 where peak A2 is expected while peak A3 and B remain essentially unaffected. The calculated DOS [Fig. 7(b)] shows that the *p*<sub>*x,y*</sub> DOS at peak A1 is slightly blueshifted when the vacancy is introduced in the apical position while, for the vacancy in the equatorial position, the *p*<sub>*z*</sub> DOS dominates in the region of peak A1 with a slight blueshift. The calculated DOS in the regions of peaks A3 and B essentially shows changes in the amplitudes with almost no chemical shift except for a substantial redshift of the *p*<sub>*x,y*</sub> DOS of peak B when the vacancy is introduced at the apical position. In contrast to these minor changes along the energy axis, the largest difference appears in the energy region between peaks A1 and A3 where a *p*<sub>*x,y*</sub> and *p*<sub>*z*</sub> DOS



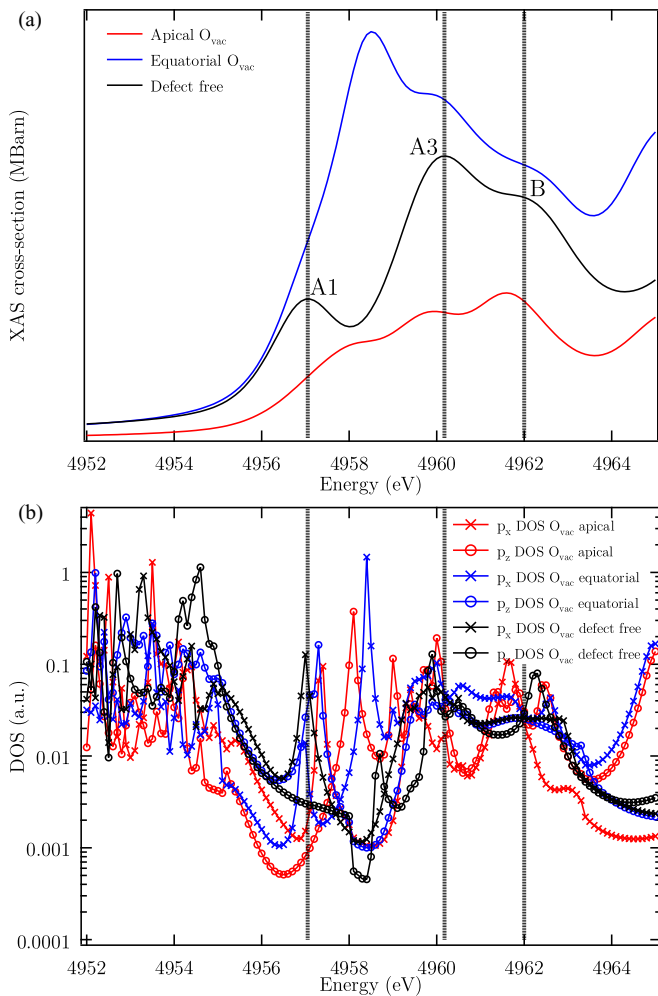


FIG. 7. (a) Effect of an oxygen vacancy introduced at the equatorial (blue) or apical position (red) of a  $\text{TiO}_6$  octahedron on the XAS spectrum of a  $4 \times 4 \times 4$  a- $\text{TiO}_2$  supercell including lattice relaxation. The spectrum at the Ti  $K$  edge for the perfect supercell is shown in black. The calculation is angle averaged (no specific orientation taken for the crystal and the incident x-ray beam). (b) Computed  $p$  DOS for defect free a- $\text{TiO}_2$  (black) and with an oxygen vacancy in the equatorial (blue) and apical position (red). The  $p_{x,y}$  DOS is shown with crosses and the  $p_z$  DOS with circles. Vertical dotted lines are guides to the eye at the energy position of the peaks maxima in the pre-edge of defect free a- $\text{TiO}_2$ .

appears upon formation of a vacancy in the equatorial and apical position, respectively. Hence, DOS is formed in the region of peak A2, which has the polarization corresponding to the orbitals pointing towards the  $\text{O}_{\text{vac}}$ . It is clear from this analysis that this DOS is representative of the defect states introduced by the  $\text{O}_{\text{vac}}$ . We have compared our calculated DOS with other authors. Janotti *et al.* report hybrid functionals calculations (HSE) which predict that  $\text{V}_\text{O}^{2+}$  forms empty DOS 0.65 eV above the conduction band minimum (CBM) [55], which is comparable to our prediction of 0.71 eV and 1.11 eV for the energy of the calculated DOS representative of  $\text{V}_\text{O}^{2+}$  with respect to the CBM. Na-Phattalung *et al.* find that the unoccupied DOS of the nearest titanium atoms to the vacancy has a maximum on the low-energy side of peak A3, in agree-

ment with our results for the vacancy in the equatorial position [56]. Similar results have been obtained in rutile  $\text{TiO}_2$  for which doubly ionized oxygen vacancies introduce a blueshift of the Ti  $3d$ -DOS by 1 eV [57]. A similar effect is present in a- $\text{TiO}_2$  at the O  $K$  edge where the asymmetry of the so-called  $t_{2g}$  and  $e_g$  peaks with a tail on the high-energy side cannot be reproduced in the calculations with a bulk structure which is assigned to the presence of blueshifted defect states from the bulk [58]. The amplitude of these peaks increases upon heavy ion irradiation compatible with the formation of more oxygen vacancies [59]. Hence, we find that the occurrence of a transition corresponding to undercoordinated Ti atoms in the region of peak A2 overlapping with the intrinsic quadrupolar transition detailed in Sec. V B is a coincidence. The experimental spectrum of a- $\text{TiO}_2$  nanoparticles with defects would be a linear combination of the  $\text{O}_{\text{vac}}$  spectra (red and blue curves in Fig. 7) and the spectrum of hexacoordinated Ti atoms in the bulk (black curve in Fig. 7), which depends on the amount of vacancy in the system. However, this study shows that peak A2 is expected to be present even in crystalline a- $\text{TiO}_2$  nanoparticles because the intrinsic quadrupolar transition is likely dominant over the defect contribution. The large increase in cross section in the region of peak A2 for pentacoordinated Ti atoms is fully compatible with our recent studies on photoexcited a- $\text{TiO}_2$  nanoparticles [25,26,29]. We therefore conclude that peak A2 originates from an essentially quadrupolar transition in the regular a- $\text{TiO}_2$  lattice and from the  $p$  DOS of pentacoordinated Ti atoms with an  $\text{O}_{\text{vac}}$  in the vicinity.

## VI. CONCLUSION

In summary, a complementary approach using experimental Ti  $K$  edge LD measurements of a- $\text{TiO}_2$  single crystals, *ab-initio* FDM calculations and spherical tensor analysis provides an unambiguous assignment of the pre-edge features. We show that A1 is mainly caused by a dipolar transition to on-site hybridized  $4p_{x,y} - 3d_{xz}, 3d_{yz}$  final states, which give a strong dipolar LD to the transition with a weak quadrupolar component from  $(3d_{xz}, 3d_{yz}, 3d_{x^2-y^2})$  states. The A3 peak is due to a mixture of dipolar transitions to hybridized  $4p_{x,y,z} - (3d_{xy}, 3d_{z^2})$  final states as a result of strong hybridization with the  $3d$  orbitals of the nearest Ti neighbor with a small quadrupolar component. The B peak is purely dipolar ( $4p$  orbitals in the final state) and is an off-site transition (the electron final state is delocalized around the absorbing atom). The distinction between on-site and off-site transitions is possible using different cluster sizes in the FDM calculations. The LD is visible well above the absorption edge due to the strong  $p$ -orbital polarization in a- $\text{TiO}_2$  which affects the amplitude of the XANES and EXAFS. Surprisingly, a quadrupolar angular evolution of peak A2 is observed for the first time with a narrow bandwidth, showing that it is an intrinsic transition of the single crystal. A connection between the unexpectedly large experimental amplitude of this peak in nanoparticles is made with oxygen vacancies forming pentacoordinated Ti atoms. Crude FDMNES calculations show that empty DOS appears in the region of peak A2 upon formation of oxygen vacancies ( $\text{V}_\text{O}^{2+}$ ) and that it overlaps with the quadrupolar transition observed in this work for defect-free materials. This

explains the relatively intense A2 peak in amorphous TiO<sub>2</sub> [24] or upon electron trapping at defects after photoexcitation of anatase or rutile TiO<sub>2</sub> [25,26,29]. The unprecedented quantitative agreement provided in this paper is made possible by the continued improvement of computational codes, including full potentials [18–20] and the more accurate description of the core-hole interaction in Bethe-Salpeter calculations [31,60]. Experiments are ongoing to extend this work to rutile TiO<sub>2</sub>.

The present results and analysis should be cast in the context of ongoing ultrafast x-ray spectroscopy studies at Free Electron Lasers [61,62]. For materials such as a-TiO<sub>2</sub>, the increased degree of detail that can be gathered from such sources was nicely illustrated in a recent paper by Obara *et al.* [27] on a-TiO<sub>2</sub>, showing that the temporal response of the pure electronic feature (at the Ti *K* edge) is much faster (~100 fs) than the response of structural features (~330 fs) such as the pre-edge and the above-edge XANES. The present work

shows that by exploiting the angular dependence of some of the spectral features, even up to the EXAFS region, one could get finer details about the structural dynamics, in particular about nonequivalent displacements of nearest neighbors.

#### ACKNOWLEDGMENTS

We thank Yves Joly and Christian Brouder for fruitful discussions and Hengzhong Zhang for providing the FDMNES input files. We also thank Beat Meyer and Mario Birri of the microXAS beamline for their technical support as well as the Bernina station staff of the SwissFEL for lending us the goniometer stage. This work was supported by the Swiss NSF via the NCCR:MUST, Grants No. 200020\_169914 and No. 200021\_175649, and the European Research Council (ERC) Advanced Grants No. H2020 ERCEA and No. 695197 DY-NAMOX. G.F.M. and C.B. were supported via the InterMUST Women Fellowship.

- 
- [1] M. Freitag, J. Teuscher, Y. Saygili, X. Zhang, F. Giordano, P. Liska, J. Hua, S. M. Zakeeruddin, J.-E. Moser, M. Grätzel, and A. Hagfeldt, *Nat. Photon.* **11**, 372 (2017).
- [2] K. Nakata and A. Fujishima, *J. Photochem. Photobiol., C* **13**, 169 (2012).
- [3] K. Suenaga, M. Tencé, C. Mory, C. Colliex, H. Kato, T. Okazaki, H. Shinohara, K. Hirahara, S. Bandow, and S. Iijima, *Science* **290**, 2280 (2000).
- [4] J. F. Sherson, C. Weitenberg, M. Endres, M. Cheneau, I. Bloch, and S. Kuhr, *Nature* **467**, 68 (2010).
- [5] C. J. Milne, T. J. Penfold, and M. Chergui, *Coord. Chem. Rev.* **277**, 44 (2014).
- [6] C. Brouder, D. Cabaret, A. Juhin, and P. Sainctavit, *Phys. Rev. B* **81**, 115125 (2010).
- [7] V. Luca, *J. Phys. Chem. C* **113**, 6367 (2009).
- [8] R. Brydson, H. Sauer, W. Engel, J. M. Thomass, E. Zeitler, N. Kosugi, and H. Kuroda, *J. Phys.: Condens. Matter* **1**, 797 (1999).
- [9] T. Uozumi, K. Okada, A. Kotani, O. Durmeyer, J. P. Kappler, E. Beaurepaire, and J. C. Parlebas, *Europhys. Lett.* **18**, 85 (1992).
- [10] Z. Y. Wu, G. Ouvrard, P. Gressier, and C. R. Natoli, *Phys. Rev. B* **55**, 10382 (1997).
- [11] D. W. Fischer, *Phys. Rev. B* **5**, 4219 (1972).
- [12] M. F. Ruiz-Lopez and A. Munoz-Paez, *J. Phys.: Condens. Matter* **3**, 8981 (1991).
- [13] L. A. Grunes, *Phys. Rev. B* **27**, 2111 (1983).
- [14] F. Farges, G. E. Brown, and J. J. Rehr, *Phys. Rev. B* **56**, 1809 (1997).
- [15] C. A. Triana, C. M. Araujo, R. Ahuja, G. A. Niklasson, and T. Edvinsson, *Phys. Rev. B* **94**, 165129 (2016).
- [16] T. Yamamoto, *X-Ray Spectrometry* **37**, 572 (2008).
- [17] D. Cabaret, A. Bordage, A. Juhin, M. Arfaoui, and E. Gaudry, *Phys. Chem. Chem. Phys.* **12**, 5619 (2010).
- [18] Y. Joly, D. Cabaret, H. Renevier, and C. R. Natoli, *Phys. Rev. Lett.* **82**, 2398 (1999).
- [19] Y. Joly, *Phys. Rev. B* **63**, 125120 (2001).
- [20] Y. Joly, O. Bunău, J. E. Lorenzo, R. M. Galéra, S. Grenier, and B. Thompson, *J. Phys.: Conf. Ser.* **190**, 012007 (2009).
- [21] L. X. Chen, T. Rajh, Z. Wang, and M. C. Thurnauer, *J. Phys. Chem. B* **101**, 10688 (1997).
- [22] V. Luca, S. Djajanti, and R. F. Howe, *J. Phys. Chem. B* **102**, 10650 (1998).
- [23] T. L. Hanley, V. Luca, I. Pickering, and R. F. Howe, *J. Phys. Chem. B* **106**, 1153 (2002).
- [24] H. Zhang, B. Chen, J. F. Banfield, and G. A. Waychunas, *Phys. Rev. B* **78**, 214106 (2008).
- [25] M. H. Rittmann-Frank, C. J. Milne, J. Rittmann, M. Reinhard, T. J. Penfold, and M. Chergui, *Angew. Chem. Int. Ed.* **53**, 5858 (2014).
- [26] F. G. Santomauro, A. Lübcke, J. Rittmann, E. Baldini, A. Ferrer, M. Silatani, P. Zimmermann, S. Grübel, J. A. Johnson, S. O. Mariager, P. Beaud, D. Grolimund, C. Borca, G. Ingold, S. L. Johnson, and M. Chergui, *Sci. Rep.* **5**, 14834 (2015).
- [27] Y. Obara, H. Ito, T. Ito, N. Kurahashi, S. Thürmer, H. Tanaka, T. Katayama, T. Togashi, S. Owada, Y.-i. Yamamoto, S. Karashima, J. Nishitani, M. Yabashi, T. Suzuki, and K. Misawa, *Structural Dyn.* **4**, 044033 (2017).
- [28] E. Baldini, L. Chiodo, A. Dominguez, M. Palummo, S. Moser, M. Yazdi-Rizi, G. Auböck, B. P. P. Mallett, H. Berger, A. Magrez, C. Bernhard, M. Grioni, A. Rubio, and M. Chergui, *Nat. Commun.* **8**, 13 (2017).
- [29] J. Budarz, F. G. Santomauro, M. H. Rittmann-Frank, C. J. Milne, T. Huthwelker, D. Grolimund, J. Rittmann, D. Kinschel, T. Rossi, and M. Chergui, *CHIMIA Int. J. Chem.* **71**, 768 (2017).
- [30] Z. Y. Wu, D. C. Xian, T. D. Hu, Y. N. Xie, Y. Tao, C. R. Natoli, E. Paris, and A. Marcelli, *Phys. Rev. B* **70**, 033104 (2004).
- [31] C. Vorwerk, C. Cocchi, and C. Draxl, *Phys. Rev. B* **95**, 155121 (2017).
- [32] See Supplemental Material at <http://link.aps.org/supplemental/10.1103/PhysRevB.100.245207> for details about the sample synthesis and characterizations, the fitting procedure, the evolution of the A2, A3, and B peaks amplitudes with  $\theta$  and  $\phi$ , the integrated DOS along ( $x, y$ ) and  $z$  axes, the XAS spectra per equivalent sites, the comparison between calculated spectra

- with space group and supercell and the crystal symmetrization of spherical tensors.
- [33] C. Brouder, A. Juhin, A. Bordage, and M.-A. Arrio, *J. Phys.: Condens. Matter* **20**, 455205 (2008).
- [34] J. Als-Nielsen and D. McMorrow, *Elements of Modern x-ray Physics* (John Wiley & Sons, Hoboken, NJ, 2011).
- [35] C. Brouder, J. P. Kappler, and E. Beaurepaire, *Proceedings of 2nd European Conference on Progress in X-ray Synchrotron Radiation Research*, Vol. 25 (SIF, Bologna, 1990), p. 19.
- [36] B. Henke, E. Gullikson, and J. Davis, *At. Data. Nucl. Data Tables* **54**, 181 (1993).
- [37] G. N. George, R. C. Prince, T. G. Frey, and S. P. Cramer, *Phys. B-Condens. Matter* **158**, 81 (1989).
- [38] G. Louprias, S. Rabii, J. Tarbès, S. Nozières, and R. C. Tatar, *Phys. Rev. B* **41**, 5519 (1990).
- [39] H. Oyanagi, M. Tokumoto, T. Ishiguro, H. Shirakawa, H. Nemoto, T. Matsushita, and H. Kuroda, *Synthetic Met.* **17**, 491 (1987).
- [40] H. Oyanagi, K. Oka, H. Unoki, Y. Nishihara, K. Murata, T. Matsushita, M. Tokumoto, and Y. Kimura, *Physica B-Condens. Matter* **158**, 436 (1989).
- [41] R. F. Pettifer, C. Brouder, M. Benfatto, C. R. Natoli, C. Hermes, and M. F. Ruiz Lopez, *Phys. Rev. B* **42**, 37 (1990).
- [42] S. Stizza, M. Benfatto, A. Bianconi, J. García, G. Mancini, and C. R. Natoli, *J. Phys. Colloques* **47**, C8-691 (1986).
- [43] C. Frétnigny, D. Bonnin, and R. Cortès, *J. Phys. Colloques* **47**, C8-869 (1986).
- [44] For a spectrum measured well above the absorption edge, the atomic background absorption converges for any incident polarization and can also be used in principle to renormalize the spectra.
- [45] R. Carboni, S. Giovannini, G. Antonioli, and F. Boscherini, *Phys. Scr.* **2005**, 986 (2005).
- [46] C. Gougoussis, M. Calandra, A. Seitsonen, C. Brouder, A. Shukla, and F. Mauri, *Phys. Rev. B* **79**, 045118 (2009).
- [47] L. Hedin and B. I. Lundqvist, *J. Phys.: Solid State Phys.* **4**, 2064 (2001).
- [48] C. Brouder, *J. Phys.: Condens. Matter* **2**, 701 (1990).
- [49] The normalization energy is at 4988.5 eV.
- [50] L. Chiodo, J. M. García-Lastra, A. Iacomino, S. Ossicini, J. Zhao, H. Petek, and A. Rubio, *Phys. Rev. B* **82**, 045207 (2010).
- [51] W. Kang and M. S. Hybertsen, *Phys. Rev. B* **82**, 085203 (2010).
- [52] B. J. Morgan and G. W. Watson, *Phys. Rev. B* **80**, 233102 (2009).
- [53] E. Finazzi, C. Di Valentin, G. Pacchioni, and A. Selloni, *J. Chem. Phys.* **129**, 154113 (2008).
- [54] The energy axis of Fig. 7 is shifted with respect to the other energy scales reported in the paper by  $\sim 12$  eV. This is because the FDMNES calculations provide a calculated spectrum which is energy shifted with respect to the experiment. A shift is applied for a straightforward comparison between calculations and experiment. This energy shift is not applied in Fig. 7. Calculations performed with the space group or with the supercell for a random polarization are shown in the Supplemental Material Fig. 11.
- [55] A. Janotti, J. B. Varley, P. Rinke, N. Umezawa, G. Kresse, and C. G. Van de Walle, *Phys. Rev. B* **81**, 085212 (2010).
- [56] S. Na-Phattalung, M. F. Smith, K. Kim, M.-H. Du, S.-H. Wei, S. B. Zhang, and S. Limpijumnong, *Phys. Rev. B* **73**, 125205 (2006).
- [57] G. C. Vásquez, S. Z. Karazhanov, D. Maestre, A. Cremades, J. Piqueras, and S. E. Foss, *Phys. Rev. B* **94**, 235209 (2016).
- [58] P. Krüger, M. Sluban, P. Umek, P. Guttman, and C. Bittencourt, *J. Phys. Chem. C* **121**, 17038 (2017).
- [59] H. Thakur, R. Kumar, P. Thakur, N. B. Brookes, K. K. Sharma, A. Pratap Singh, Y. Kumar, S. Gautam, and K. H. Chae, *J. Appl. Phys.* **110**, 083718 (2011).
- [60] E. L. Shirley, *J. Electron Spectrosc. Relat. Phenom.* **136**, 77 (2004).
- [61] R. Abela, P. Beaud, J. A. van Bokhoven, M. Chergui, T. Feurer, J. Haase, G. Ingold, S. L. Johnson, G. Knopp, H. Lemke, C. J. Milne, B. Pedrini, P. Radi, G. Schertler, J. Standfuss, U. Staub, and L. Patthey, *Structural Dyn.* **4**, 061602 (2017).
- [62] M. Chergui, *Structural Dyn.* **3**, 031001 (2016).